Response Letter

Manuscript Title: Wind speed estimation using second-order sliding-mode observers: simulation and experimental validation on a floating offshore wind turbine

Manuscript Number: wes-2025-206

Overall Response:
The authors would like to thank the esteemed editor-in-chief and reviewer for their invaluable comments. We do appreciate the time the reviewer put into reviewing our paper. The paper has been revised according to the reviewer's comments.
The reviewer's main suggestion pertains to integrating wind estimation with a controller. To clarify our decision, the authors have deliberately chosen to focus exclusively on the observer design in this work. Several key original contributions underpin this decision:

i) **Rigorous observability analysis:** To the best of our knowledge, this analysis has not been explored in previous research, providing a solid theoretical foundation for the design of our observer.

ii) **A novel and promising observation solution:** The observer solution proposed offers significant advancements including:

- **Adaptive gains:** The proposed approach simplifies the tuning process by incorporating adaptive gains, which enhance flexibility and reduce the complexity of the tuning process.
- **Finite-time convergence:** The system guarantees finite-time convergence thanks to the theory of sliding mode, which is a important point.
- **Robustness:** The observer has been designed to be robust to model uncertainties and external disturbances.
- **Stability guarantee:** The observer ensures stability, which is critical for the reliable operation of the control system.

iii) Furthermore, the current work (not yet published) shows the efficiency of the closed-loop system, which incorporates both the adaptive observer and adaptive controller, along with a formal proof of the stability of the observer-based control approach.

A marked-up version of the revised manuscript is attached at the end of this response letter. Below, we provide a detailed, point-by-point response to each reviewer's comments.

- The reviewer's comment to the authors is presented in BLACK.
- Authors' responses to the reviewer's comments are presented in BLUE.
- Those parts of the paper that have been changed are addressed in the authors' responses and are presented in RED.

Response to Referee #1

The paper proposes a novel second order sliding mode observer (SOSMO) for wind estimation on floating off shore wind turbines. Two methods are introduced and compared with the extended Kalman filter (CD-EKF) available in ROSCO. Simulation studies with FAST and Turbsim show that the SOSMO observers can produce wind estimates with smaller RMS error than those from CD-EKF. The results are further validated on a FOWT in laboratory-scale software in the loop experiments. Three wind profiles are considered and in each case the SOSMO observers again achieve smaller RMS errors than CD-EKF.

The paper is clearly written and the motivation is clear. Some comments:

1. The reference for Lidar (Jena and Rajendran, 2015) is now rather dated. The use of Lidar for WTC has been extensively investigated and was the subject of the IEA Wind Task 32. The authors are recommended to view their publications on the utility of Lidar for turbine control, available from `https://zenodo.org/communities/ieawindtask32/about` and use these to provide a more contemporary assessment on the utility of Lidar for WTC.

   Response: We thank the reviewer for the suggestion. Following this recommendation, we agree that the literature review can be improved, specifically regarding Lidar-assisted wind turbine control. We have therefore reviewed key publications from IEA Wind Task 32 and incorporated several relevant and more recent references into the revised manuscript.
   The updated text in the introduction now highlights contemporary findings regarding the benefits and limitations of Lidar for control. These additions offer a more complete and modern assessment of the role of Lidar in WTC.
   The manuscript has been updated accordingly as follows:

   LiDAR use. An advanced remote sensor-based method commonly used is light detection and ranging (LiDAR) which can sample the wind field upstream of the turbine to provide a measurement of upstream wind speed (Harris et al., 2006; Shu et al., 2016). A considerable amount of literature has demonstrated the potential of LiDAR-assisted control for performance improvement and load mitigation in wind turbines such as (He et al., 2025; Moldenhauer and Schmid, 2025; Li and Geng, 2024; Guo and Schlipf, 2023; Mahdizadeh et al., 2021; Schlipf et al., 2023; Guo et al., 2023). Simley et al. (2020) provide an overview of recent advances and open problems in the use of LiDAR for enhancing wind turbine operation and control. Despite the significant progress achieved in this area, some practical limitations remain. One of the most apparent limitations is the

cost and the maintenance demand of these systems (Jena and Rajendran, 2015; Woolcock et al., 2023). LiDAR devices, particularly those used in offshore and floating structures, are expensive to acquire and install, and their operation in harsh marine environments imposes high standards on longevity, autonomous operation, and regular maintenance to guarantee data quality. In addition, a primary technical limitation lies in the vulnerability of LiDAR measurements to motion-induced errors. Floating platform motions distort the LiDAR's line of sight~~, introducing systematic biases and increased uncertainty in wind speed estimation~~ and also the apparent wind speed because of the LiDAR translation, introducing systematic biases and increased uncertainty in wind speed estimation (Gräfe et al., 2023). Such disturbances can lead to errors in real-time control. Moreover, LiDAR measurements inherently suffer from limited correlation with the actual wind field impacting the rotor, since wind is measured several rotor diameters upstream and evolves due to turbulence, while volume averaging and point-wise sampling prevent reconstruction of the exact rotor-scale wind field, introducing unavoidable uncertainty in the measured REWS (Svenstrup and Thomsen, 2024).

2. The discussion of computation time is too brief, what does runtime refer to? The computation for the convergence time for each algorithm needs to be shown, to enable comparisons of their suitability for real-time control implementation.

   Response: We thank the reviewer for this comment.
   We now explicitly state that the reported runtime refers only to the CPU time required by each observer block, as measured using the MATLAB/Simulink Profiler (R2023a). Although a full 800-s simulation takes for example x seconds of real time, the majority of this cost arises from OpenFAST and other modules. The profiler allows isolating the execution time of each observer, independent of the plant model, and the values reported in the manuscript correspond solely to the computations performed inside each estimator. To clarify this in manuscript, the following text is added (page 21 of the revised version):

4.4 Computational time

To assess the computational burden associated with each observer, the execution time of every estimator block using the MATLAB/Simulink Profiler (R2023a) is measured. Importantly, the reported run-time refers exclusively to the time required for the internal computations of each observer. All measurements are obtained under identical conditions (Sect. 4.1), ensuring fair comparison. The CD-EKF exhibited the longest run-time (18 ms), followed by the ASOSMO (11 ms) and the SOSMO (9 ms). These results reflect the higher algorithmic complexity of the CD-EKF, as expected. The ASOSMO slightly increases complexity with its adaptive gain mechanism, in contrast to the constant gain used in the SOSMO (see Fig. 10).

To complement the discussion on computational time and to address the reviewer's request, an additional study has been conducted to evaluate the robustness of each observer

when initialized with different initial condition of estimators. The following text has been added to page 18 of the revised version.

4.3 Monte Carlo analysis

In this experiment, *the only quantity varied from run to run is the initial condition of the observers*. All other components of the simulation, including the turbulent wind field, wave excitation, OpenFAST dynamics, and control inputs, are kept identical across all MC realizations. Consequently, any observed variation in transient behavior is solely attributable to different initial observer states. A set of $N = 100$ simulations is generated by initializing the wind and rotor speed estimates within a uniform $\pm 30\%$ interval around their true values. Three initialization scenarios are examined: (i) rotor speed initialization error only, (ii) wind speed initialization error only, and (iii) simultaneous initialization errors in both wind speed and rotor speed.

To compare the observers consistently, a *window convergence time* is used. Convergence is declared when the worst-case estimation error across all MC runs remains within a prescribed tolerance band for a continuous duration of $T_{\text{hold}} = 20$ s. The thresholds are chosen as $\varepsilon_\omega = 0.2$ rad/s for rotor speed and $\varepsilon_v = 1.7$ m/s for wind speed. The convergence time for wind speed is defined as the earliest time at which every MC trajectory satisfies the inequality $\Delta v \leq \varepsilon_v$ for all t in a window of length T_{hold}. rotor speed convergence is defined analogously. Requiring convergence over the entire simulation would be unnecessarily restrictive. Turbulent wind excitation, platform motion, and nonlinear aerodynamic effects naturally cause short-lived error fluctuations even after the estimator has converged. The windowed criterion avoids misclassifying such fluctuations as divergence and better reflects practical control requirements.

The resulting convergence times for SOSMO, ASOSMO, and CD–EKF across all scenarios are reported in Table 2 and illustrated in Fig. 9. This metric captures the earliest time after which *all* realizations remain within the prescribed bounds.

The error-band plots show the dispersion of estimation errors caused solely by changes in initial observer states. In all scenarios, *all observers converge*. rotor speed errors settle quickly because ω is directly measured, which justifies the smaller threshold ε_ω. wind speed estimation is more difficult because v is unmeasured and its dynamics are unknown. As a result, wind speed error bands are wider and the threshold ε_v must be larger.

From Fig. 9, it can be seen that the CD–EKF typically drives the estimation error toward zero more rapidly during the initial transient. However, when applying the windowed convergence criterion—which requires the estimates to remain within the prescribed bounds for a continuous duration—the SOSMO achieves the shortest convergence times in most scenarios. This difference arises because the adaptive law in the ASOSMO starts with a conservative gain that increases only after sufficient excitation, leading to a slower approach to steady-state accuracy. In contrast, the SOSMO and CD–EKF employ fixed gains or explicit covariance updates, allowing them to settle more quickly once the estimation

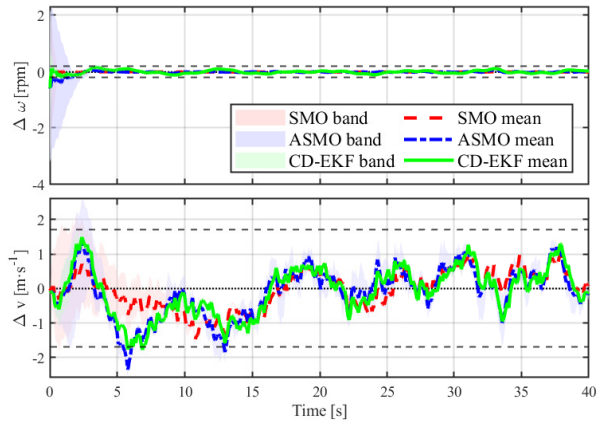

(a) $\Delta\omega_0$ only

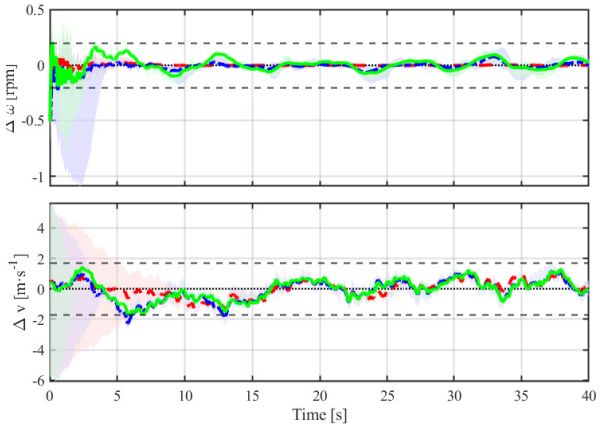

(b) Δv_0 only

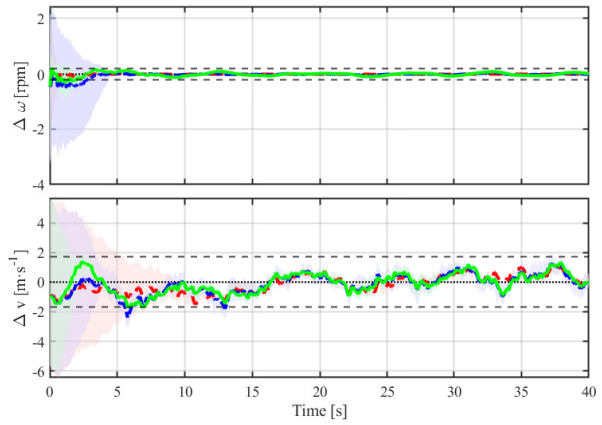

(c) $\Delta\omega_0 + \Delta v_0$

Figure 9: MC analysis with $N = 100$ realizations *per scenario* for the three initial-condition error cases.

error enters the tolerance band. Overall, while the CD–EKF is fast in the early transient, the SOSMO exhibits the most favorable worst-case convergence times under the robustness metric used here, whereas the ASOSMO consistently requires longer convergence due to its gain adaptation mechanism.

Table 2: Convergence times for rotor speed and wind speed estimation under the three initial-condition *initialization* scenarios. Each value corresponds to the earliest time at which all MC realizations for $N = 100$ remain within the prescribed error bounds.

	Rotor speed convergence times			Wind speed convergence times		
Scenario	SOSMO	ASOSMO	CD–EKF	SOSMO	ASOSMO	CD–EKF
$\Delta\omega_0$ only	0.65	3.79	1.70	2.80	13.16	6.96
Δv_0 only	2.48	3.81	3.98	10.84	13.25	13.03
$\Delta\omega_0 + \Delta v_0$	2.55	9.90	5.74	10.89	13.25	13.06

3. In the SIL experiments, the wind speed error is $v - \hat{v}$, but I didn't see an explanation of how the actual wind speed v was obtained.

   Response: Thank you for highlighting this point. The experimental setup is designed to reproduce the coupled aero, hydro, servo, and elastic behavior of a floating wind turbine under realistic physical disturbances. In the wave tank, the hydrodynamic effects, including platform motions, mooring system dynamics, and wave-induced loads, are obtained physically using the scaled prototype. Aerodynamic effects are emulated in real time through a software-in-the-loop (SIL) implementation of OpenFAST. In this configuration, OpenFAST computes the aerodynamic forces corresponding to a prescribed wind field, and these forces are applied to the physical model via the six-component thrust generator mounted on the tower.
   Therefore, the inflow wind acting on the turbine is defined numerically. The wind signal $v(t)$ used in the SIL simulation is therefore the only wind field that determines the aerodynamic loads applied to the physical structure. For this reason, the reference wind speed $v(t)$ used in our analysis (including the computation of $v(t) - \hat{v}(t)$) is taken directly from the wind input provided to OpenFAST.
   We have added a detailed explanation in Section 5 of the revised manuscript regarding the SIL test setup and how the reference wind speed $v(t)$ is defined in this environment, and we have also included a new schematic (Fig. 12) to clearly illustrate the interaction between the numerical OpenFAST modules and the physical wave-tank experiment.

5 Experimental results

The proposed observers have been experimentally validated on a SIL setup at École Centrale Nantes, France. The experimental platform consists of a 1/32-scale semi-submersible FOWT, based on the OC4-DeepCwind concept, deployed in the wave tank of the LHEEA Laboratory (LHEEA Laboratory, 2025). The physical model includes the floating platform, tower, and mooring system and is instrumented with motion-tracking markers and load sensors, as shown in Fig. 10. This setup provides realistic hydrodynamic excitation through physical wave generation and platform motion.

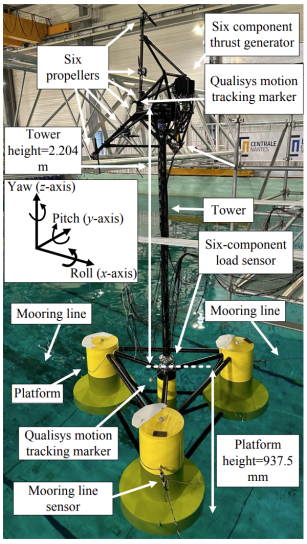

Figure 11: Experimental SIL test setup of the 5 MW 1/32-scale semi-submersible OC4 FOWT at *École Centrale Nantes* (Aslmostafa et al., 2026).

The overall SIL architecture is illustrated in Fig. 12. In this hybrid configuration, the hydrodynamic processes, wave excitation, viscous and radiation loads, mooring-line forces, and the resulting platform dynamics are reproduced physically in the wave tank. Consequently, the corresponding hydrodynamic modules of OpenFAST (HydroDyn, MAP++, MoorDyn or FEAMooring, ElastoDyn), highlighted in the blue dashed region of Fig. 12, are disabled in the numerical simulation. Instead, the measured 6 degrees of freedom platform and tower-top motions from the Qualisys system are imposed as inputs to the real-time numerical model (Bonnefoy et al., 2024). It should be noted that aerodynamic loads are computed numerically. In other words, a modified real-time implementation of OpenFAST runs, where the wind field is prescribed numerically and the aerodynamic modules (InflowWind, AeroDyn, ServoDyn), highlighted in the red dashed region of Fig. 12, remain active. At each iteration of the SIL loop, the solver receives the measured motions and computes the instantaneous aerodynamic thrust corresponding to the imposed wind field. This thrust is then applied to the physical model by a tower-top actuator system (Fig. 11), enabling consistent aero-hydro coupling during the experiment.

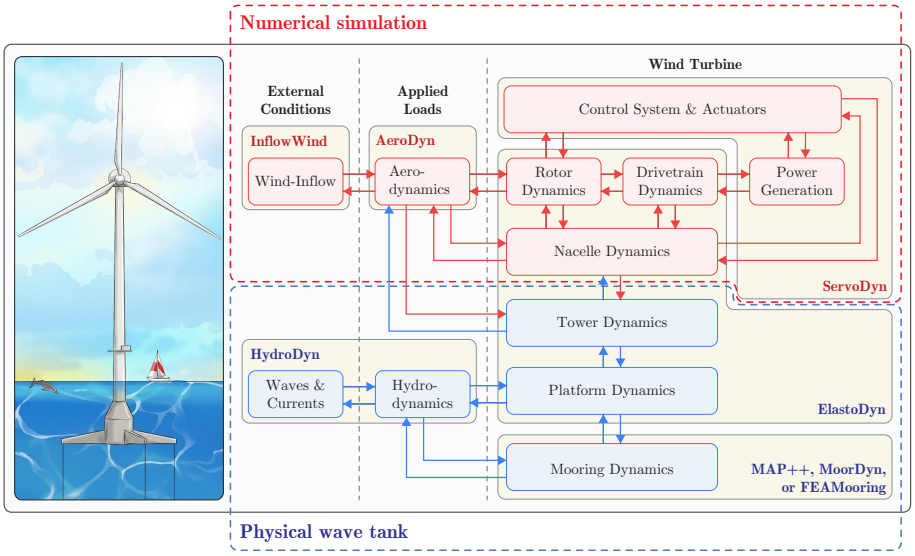

Figure 12: Schematic of the modules in the SIL architecture. The figure is inspired by Bonnefoy et al. (2024) and National Renewable Energy Laboratory (2023). The hydrodynamic and structural modules (blue dashed region) are disabled, as the corresponding processes are reproduced physically in the wave tank, while the aerodynamic modules (red dashed region) remain active and compute real-time aerodynamic loads using the prescribed wind field and measured platform motions.

In the SIL setup, the inflow wind field is numerically prescribed in OpenFAST. Based on this inflow and the instantaneous platform and rotor conditions, OpenFAST computes the corresponding REWS $v_r(t)$, which is used as the reference signal for evaluating the estimation error.This approach allows the observer to be tested under realistic platform motions and hydrodynamic conditions, i.e., under realistic physical disturbances.

4. The use of rotor speed to estimate wind speed has been investigated for quite some time, see for example the survey in Soltani, et al Estimation of REWS: A Comparison, TCST 2013 `https://doi.org/10.1109/TCST.2013.2260751` Due to their highly stochastic nature, all wind estimates requires low pass filtering before they can be used for control purposes. Indeed, it is clear from Figure 11-13 that all three estimation methods filter the wind. The important question is how well they preserve the portion of the spectrum that is useful for control, and RMS error may not be a good measure for this.

   Response: We thank the reviewer for this comment. We agree that using RMS-based metrics alone may not sufficiently capture estimator performance.
   To address this point and strengthen the analysis, we have extended the performance evaluation by introducing additional complementary metrics in both the time-domain statistical metrics and frequency domains. These metrics provide a fairer comparison among the considered estimation methods.

   Let $x(k)$ denote the true signal (either rotor speed $\omega(k)$ or wind speed $v(k)$), $\hat{x}(k)$ its estimate, and $e(k) = \hat{x}(k) - x(k)$ the estimation error $\{e(k)\}_{k=1}^{N}$ at sample $k = 1, \ldots, N$.

   1. Root Mean Square Error (RMSE)

The root mean square error is defined as

$$\text{RMSE} = \sqrt{\frac{1}{N}\sum_{k=1}^{N} e(k)^2}.$$

2. Mean estimation error

The mean error (or bias) μ_e that indicates systematic over- or underestimation is given by $\mu_e = \mathbb{E}[e] \approx \frac{1}{N}\sum_{k=1}^{N} e(k)$.

3. Variance of estimation error

The variance of the estimation error σ_e^2 that measures how much the error fluctuates around its mean. It is a measure of the *noise level* or *spread* of the error.is

$$\sigma_e^2 = \text{Var}(e) \approx \frac{1}{N-1}\sum_{k=1}^{N}\big(e(k) - \mu_e\big)^2.$$

4. Mean Square Error (MSE)

The mean square error (MSE) which combines both variance and bias into a single scalar is defined as

$$\text{MSE} = \mathbb{E}[e^2] \approx \frac{1}{N}\sum_{k=1}^{N} e(k)^2.$$

Using μ_e and σ_e^2 one can write $\text{MSE} = \sigma_e^2 + \mu_e^2$.

6. Power Spectral Density (PSD) of the Error

The (one-sided) power spectral density (PSD) of the estimation error which shows how the error energy is distributed across frequencies is denoted by $S_e(f)$, where f is frequency. As a theoretical continuous-time quantity, the PSD is defined via the finite-time Fourier transform of $e(t)$ as

$$S_e(f) = \lim_{T\to\infty} \frac{1}{T}\left|\int_0^T e(t)\, e^{-j2\pi f t}\, dt\right|^2.$$

In practice, $S_e(f)$ is estimated from the sampled error sequence $e(k)$ using Welch's method, as implemented in MATLAB's `pwelch` function.

Following Soltani et al., we plot the frequency-weighted PSD

$$f \cdot S_e(f),$$

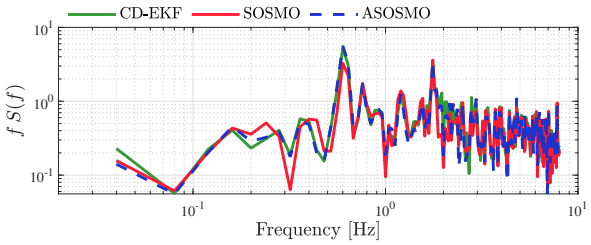

(a) Case #1

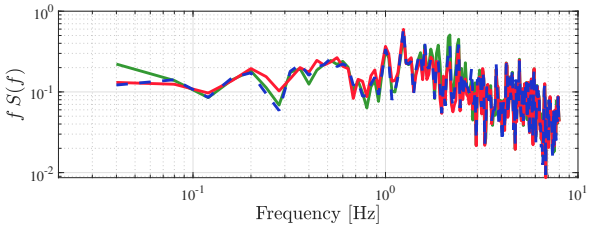

(b) Case #2

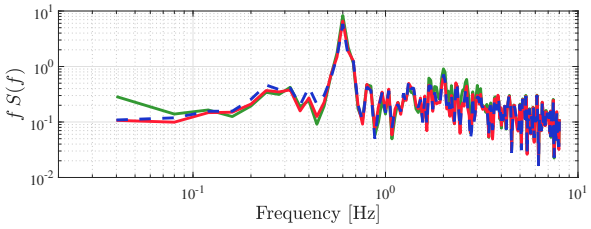

(c) Case #3

Figure 16: Power spectral density (PSD) of the REWS estimation error in three test cases.

7. Error Distribution and Gaussian Fit

To further characterize the estimation error, we plot the empirical probability distribution of $e(k)$ as a normalized histogram and compare it with a Gaussian probability density function

$$p_{\text{Gauss}}(e) = \frac{1}{\sqrt{2\pi}\,\sigma_e} \exp\left(-\frac{(e-\mu_e)^2}{2\sigma_e^2}\right),$$

using the sample mean μ_e and variance σ_e^2.

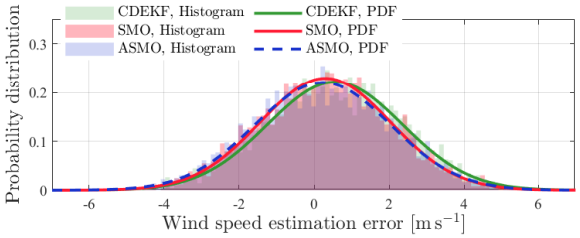

(a) Case #1

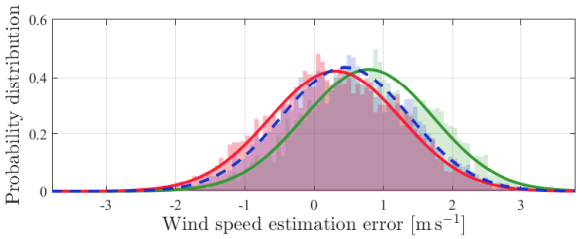

(b) Case #2

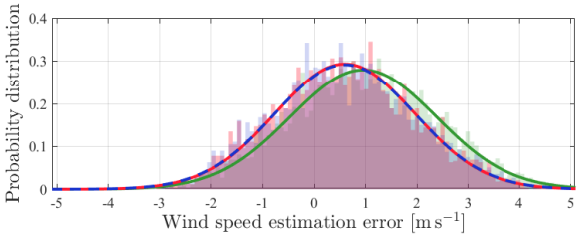

(c) Case #3

Figure 17: Comparison of the distribution and probability density function (PDF) of the REWS estimation error in three test cases.

Table 5: Time-domain statistical performance metrics for CD-EKF, SOSMO, and ASOSMO across three experimental test cases, evaluated for rotor speed ω_r and REWS v_r.

Case	**Variable**	**Method**	**RMSE**	$\mathbb{E}[e]$	σ_e^2	$\mathbb{E}[e^2]$
Case 1	ω_r	CD-EKF	9.00×10^{-2}	-1.29×10^{-2}	7.93×10^{-3}	8.09×10^{-3}
		SOSMO	5.90×10^{-2}	1.42×10^{-3}	3.48×10^{-3}	3.48×10^{-3}
		ASOSMO	1.14×10^{-1}	-6.64×10^{-3}	1.30×10^{-2}	1.30×10^{-2}
	v_r	CD-EKF	1.89	5.54×10^{-1}	3.25	3.56
		SOSMO	1.76	3.02×10^{-1}	3.02	3.11
		ASOSMO	1.84	2.41×10^{-1}	3.32	3.38
Case 2	ω_r	CD-EKF	6.74×10^{-2}	-4.82×10^{-3}	4.53×10^{-3}	4.55×10^{-3}
		SOSMO	2.40×10^{-2}	1.68×10^{-5}	5.75×10^{-4}	5.74×10^{-4}
		ASOSMO	4.49×10^{-2}	-2.80×10^{-3}	2.00×10^{-3}	2.01×10^{-3}
	v_r	CD-EKF	1.22	7.87×10^{-1}	8.66×10^{-1}	1.49
		SOSMO	9.93×10^{-1}	3.08×10^{-1}	8.92×10^{-1}	9.86×10^{-1}
		ASOSMO	1.02	4.56×10^{-1}	8.41×10^{-1}	1.05
Case 3	ω_r	CD-EKF	7.52×10^{-2}	-2.98×10^{-3}	5.65×10^{-3}	5.66×10^{-3}
		SOSMO	4.27×10^{-2}	6.36×10^{-4}	1.83×10^{-3}	1.83×10^{-3}
		ASOSMO	5.20×10^{-2}	-7.48×10^{-5}	2.70×10^{-3}	2.70×10^{-3}
	v_r	CD-EKF	1.72	9.57×10^{-1}	2.04	2.96
		SOSMO	1.49	5.98×10^{-1}	1.85	2.21
		ASOSMO	1.49	5.96×10^{-1}	1.88	2.23

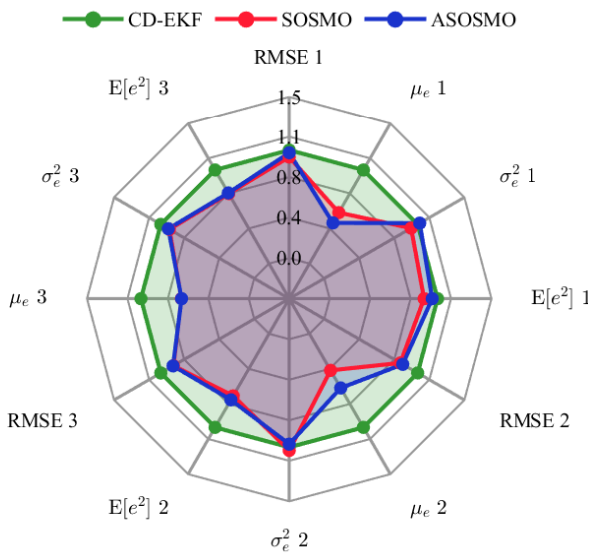

Figure 18: Comparison of normalized error metrics for the three REWS estimation methods: CD–EKF, SOSMO, and ASOSMO, evaluated over three representative wind cases. All metrics are normalized with respect to the CD–EKF baseline.

5. Ultimately, the real test of a wind speed estimate is its utility for WTC, and this aspect of REWs has been extensively investigated in several recent papers, notably Guo, F. et al Evaluation of lidar-assisted wind turbine control under various turbulence characteristics, WES 2023 `https://doi.org/10.5194/wes-8-149-2023` and the cited WES paper by Moldenhauer 2025. These papers discussed many features of wind estimation and filtering for their implementation within control methodologies. The wind estimation methods were then combined with novel control methodologies to deliver improved WTC control for turbine fatigue load reduction.

   Response: We thank the reviewer for highlighting the importance of assessing wind speed estimation in the context of wind turbine control (WTC). We agree that recent studies, such as Guo et al. (2023) and Moldenhauer et al. (2025), provide valuable insights into how REWS estimation and preview filtering influence closed-loop load reduction.
   In the present manuscript, however, we deliberately focus on the *observer design* problem and on establishing a robust and computationally efficient wind speed estimator. This choice is motivated by the following key contributions, which we believe are meaningful on their own: (i) a rigorous observability analysis for estimating wind speed from rotor speed measurements in the considered setting; and (ii) the introduction and validation of constant-gain and adaptive second-order sliding-mode observers featuring finite-time convergence, straightforward tuning, and robustness/stability guarantees without model linearization.
   Furthermore, the current work of the authors (not yet published) shows the efficiency of the closed-loop system, which incorporates both the adaptive observer and adaptive controller, along with a formal proof of the stability of the observer-based control approach.

6. Overall, the study is interesting and well presented, but the contribution is rather limited in scope and insufficient for a strong journal like WES. In its present form, it would be well suited to a conference presentation like WESC or Torque. If the authors wish to extend their work, they may consider combining SOSMO wind estimation with WTC methods (possibly combining it with Lidar) and demonstrating improvements in some aspects of turbine control performance.

   Response: We respectfully thank the reviewer for this perspective. While the present work does not investigate a full wind turbine control loop, its contribution is focused. To the best of the authors' knowledge, this is the first study to conduct a formal observability analysis for estimating wind speed from rotor speed in the FOWT context, a question that is rarely addressed in the literature despite its conceptual importance.
   Furthermore, the paper introduces two novel observer architectures, a constant-gain and an adaptive second-order sliding-mode observer, that provide robust, non-linear, model-insensitive wind speed estimation without requiring linearization or covariance tuning. The observers also offer *finite-time convergence* properties and significantly reduced computational burden, which are highly desirable for real-time offshore applications.
   The objective of this manuscript is to establish a solid and rigorous estimation framework, validated through both high-fidelity OpenFAST simulations and SIL experiments. We believe that this constitutes a meaningful step forward and an independent scientific contribution aligned with the scope of Wind Energy Science.
   Nevertheless, we appreciate the reviewer's suggestion, and as noted above, integration of the proposed estimators into full WTC schemes represents a direction for future work.

Response to Referee #2

General comments

The article is overall well-written and structured. It is commendable to have a theoretical study of the observer as well as an experimental evaluation. Addressing the three turbine operational regimes is also of interest. A few elements could be improved and a few parts would benefit from more details as suggested below. In particular, more details on the tuning of the observers would be welcome so that the community can more easily reproduce and compare results. The prospect of connecting the observers with a control strategy in the future is interesting and would nicely complement this work.

Response: We thank the reviewer for the assessment of the manuscript and for the constructive comments. Below, we respond to the reviewer's remarks point by point and indicate the corresponding clarifications and additions made in the revised manuscript.

Specific comments

1. Throughout the document, "wind speed" is mentioned as-is when it is (most likely) free-wind speed (a.k.a. free-flow wind speed) that the authors want to estimate. Given that turbines have an induction zone with altered wind properties, it should be specified in the introduction (and abstract, possibly title too) that this study addresses *free* wind throughout.

   Response: We thank the reviewer for pointing out the importance of distinguishing between the free-stream wind and the wind speed acting on the rotor. We clarify that the objective of this work is to estimate the REWS rather than the free-stream wind speed, and this terminology is now used consistently throughout the revised manuscript, as is common in wind speed estimation studies (e.g. Soltani et al. (2013); Moldenhauer and Schmid (2025)).
   In the revised manuscript, Eq. (1) now explicitly uses the free-stream (upstream) wind speed v_∞, following standard aerodynamic references, whereas the aerodynamic torque and the remaining equations use the REWS v_r. These two wind speed quantities are now clearly defined in Sect. 2.1 on page 5 as follows:

   Wind turbines harness the kinetic energy of the wind to generate mechanical power through aerodynamic interaction between the wind and the rotating blades. The theoretical power available in the wind stream is given by

   $$P_{\text{wind}} = \frac{1}{2}\rho\pi R^2 \cancel{v^3} v_\infty^3 \tag{1}$$

   where ρ is the air density, R is the rotor radius, and ~~v is the wind speed upstream of the rotor~~ v_∞ denotes the free-stream (upstream) wind speed (Burton et al., 2011). However, only a portion of this energy can be converted into mechanical power owing to fundamental aerodynamic limits, ~~such as~~ reported by Betz's law (Manwell et al., 2009). The efficiency of this conversion is described by the power coefficient C_p, which quantifies the fraction of

the wind's kinetic energy that is captured by the rotor. As a consequence, aerodynamic power P_a and torque τ_a read as

$$P_a = \frac{1}{2}\rho\pi R^2 C_p\left(\lambda,\beta\right) v^3 v_r^3 \tag{2}$$

$$\tau_a = \frac{P_a}{\omega_r} \tag{3}$$

where ω_r is the rotor speed, v_r denotes the rotor–effective wind speed, and the power coefficient $C_p(\lambda,\beta)$ is a nonlinear function of the tip-speed ratio λ and the blade pitch angle β, as depicted in Fig. 1.

2. line 43: motion not only distorts the lines of sight but also the apparent wind speed because of the lidar translation.

   Response: We thank the reviewer for this helpful observation.The sentence on line 43 has been updated accordingly (on page 2, as below:

   Floating platform motions distort the LiDAR's line of sight~~, introducing systematic biases and increased uncertainty in wind speed estimation~~ and also the apparent wind speed because of the LiDAR translation, introducing systematic biases and increased uncertainty in wind speed estimation (Gräfe et al., 2023).

3. 90: specify motivation for proposing a 2nd-order observer instead of first-order one.

   Response: We appreciate the reviewer's comment. The manuscript now clarifies that the motivation for adopting a second-order sliding mode instead of a first-order one stems from the need for a continuous correction signal in FOWT applications, where rapidly varying aerodynamic and structural loads amplify the effects of the discontinuous injection inherent to first-order sliding modes. Second-order formulations, such as the supertwisting algorithm, retain the finite-time convergence of sliding-mode designs while significantly reducing chattering through a continuous control action. This rationale has been explicitly incorporated into the revised text on page 4 as follows:

   Observer based on sliding mode theory. Among observer-based approaches, sliding mode observers (SMOs) have attracted significant attention due to their inherent robustness to uncertainties and disturbances, which are particularly prevalent in offshore environments. The idea of SMO is one of driving the estimated states to properly chosen constraints (the sliding manifold) in finite time and then maintaining the sliding mode for all subsequent times so that the state estimation errors are driven to zero, thus exploiting the main features of the sliding mode: its insensitivity to external and internal disturbances matched to the control and finite-time reaching transient. Unlike KFs, which rely heavily on accurate statistical models and noise characteristics, SMOs exploit the system's nonlinear structure and discontinuous logic to force estimation errors to converge in finite time (Ma et al., 2024). This makes them well-suited for FOWTs, where system dynamics are often poorly known and subject to unpredictable perturbations. ~~Furthermore,~~

~~recent studies have demonstrated the potential of higher-order sliding mode observers to achieve estimation even in the presence of uncertainties, while reducing the negative effect (chattering) induced by discontinuity appearing in the correction term.~~ However, these insensitivity/robustness properties come at a cost, the so-called *chattering* (Levant, 2010), resulting from a high-frequency switching signal and the inevitable presence of unmodeled dynamics. These limitations have motivated higher-order sliding-mode formulations, which reduce chattering by enforcing that the sliding variable and its time derivatives, up to system relative degree (Isidori, 1989), converge to zero, thereby improving accuracy. One of the most popular techniques specifically designed for this purpose is the so-called supertwisting algorithm (Levant, 1993), which is a second-order sliding mode algorithm. It generates a robust, continuous observer while driving a sliding variable of relative degree one to the second-order sliding mode in finite time.

4. 142: specify that omega is replaced by lambda and its expression from (4).

   Response: Thank you for the comment. We have added a sentence clarifying that ω_r is replaced using $\omega_r = (\lambda\, v_r)/R$ obtained from Eq. (4).

5. 179: delta(t) having no influence on observability: is it a strong assumption? Can its validity be checked somehow? Consider elaborating on this.

   Response: Thank you for the comment. This assumption is standard and it is not strong one by a practical point of view. Numerical evaluations based on experimantal/OpenFAST data also confirm that the observability criterion is satisfied independently of $\delta(t)$.

6. 186: lambda is now lambda(omega,v), consider aligning and stabilizing your notation across equations.

   Response: Thank you for this comment. In the observability analysis, we now explicitly write $\lambda = \lambda(\omega_r, v_r)$ in order to emphasize its dependence on the rotor speed and the REWS, in accordance with Eq. (4). For the remainder of the paper, we keep the shorthand notation λ for readability, and we have added a short clarification to state this convention right after Eq. (4).

7. 188–189: consider reformulating or correcting the first sentence.

   Response: We have revised the sentence to improve clarity on page 9 as

   ~~The previous property is evaluated if $\mathbf{\Phi}_{\delta(t)=0}$ can be inverted that is a very hard task~~ Checking whether $\mathbf{\Phi}_{\delta(t)=0}$ is invertible is difficult in practice; ~~It is why~~ therefore, the previous definition can be reformulated by the next equivalent one.

8. 197–198: several steps are skipped from “det(...) not equal to 0” to “partial derivative of y-dot wrt v not equal to zero”, which may confuse readers. Agree with (15).

Response: Thank you for this comment. We have now added a short explanation showing how the Jacobian structure leads to the requirement that only $\partial \dot{y}/\partial v_r \neq 0$ must hold. This clarification has been inserted directly before Eq. (15) on page 9 as follows

~~Applying Eq. (13) to Eq. (14), it is obvious that the first line of the Jacobian $\partial \boldsymbol{\Phi}/\partial \boldsymbol{x}$ equals [1 0].~~

The Jacobian of $\boldsymbol{\Phi}$ with respect to the state vector $\boldsymbol{x}$ reads

$$\frac{\partial \boldsymbol{\Phi}}{\partial \boldsymbol{x}} = \begin{bmatrix} \frac{\partial y}{\partial \omega_r} & \frac{\partial y}{\partial v_r} \\ \frac{\partial \dot{y}}{\partial \omega_r} & \frac{\partial \dot{y}}{\partial v_r} \end{bmatrix} = \begin{bmatrix} 1 & 0 \\ \frac{\partial \dot{y}}{\partial \omega_r} & \frac{\partial \dot{y}}{\partial v_r} \end{bmatrix}. \tag{15}$$

Therefore, the generic observability condition $\det(\partial \boldsymbol{\Phi}/\partial \boldsymbol{x}) \neq 0$ is equivalent to requiring that $\partial \dot{y}/\partial v_r \neq 0$.

9. 216: "double integrator": consider introducing this choice with more justification.

   Response: We thank the reviewer for this comment. In response, a clarification has been added to the manuscript explaining why the dynamics in Eq. (20) can be classified as a perturbed double–integrator system. After the coordinate transformation, the state variables become $(z_1, z_2) = (y, \dot{y})$, which yields $\dot{z}_1 = z_2$. The remaining dynamics enter solely through the second equation as an additive term that aggregates model uncertainties, nonlinear aerodynamic effects, and disturbances. This produces the canonical chain–of–integrators structure widely used in nonlinear control, where the system behaves as two cascaded integrators driven by an uncertain but bounded input. Such a structure directly motivates the adoption of finite–time robust observers such as the supertwisting algorithm. The following sentence has been added to the manuscript to make this explicit:

   It should be noted that the structure in Eq. (20) corresponds to a perturbed double-integrator system. Indeed, the coordinate transformation in Eq. (17) yields $z_1 = y$ and $z_2 = \dot{y}$, so that $\dot{z}_1 = z_2$. All model uncertainties and unmeasured effects appear as an additive term in the second equation, namely $\dot{z}_2 = \mathcal{F}(\cdot)$. Therefore, the linear part of the dynamics corresponds to the standard chain-of-integrators form.

10. 216: "supertwisting": if that name can help get a better understanding, consider explaining it.

    Response: We thank the reviewer for this comment. The term "supertwisting" originates from the classical twisting algorithm in sliding-mode control. The twisting algorithm is a second-order sliding-mode method whose behavior is commonly interpreted in a phase-plane framework involving the sliding variable and its derivative, resulting in a characteristic twisting motion around the sliding manifold (Levant, 1993).
    The supertwisting algorithm, a name introduced by Levant (2003), can be viewed as an extension of the twisting concept. It is a second-order sliding-mode algorithm that achieves

finite-time convergence of the sliding variable without requiring explicit measurement of its derivative, while preserving robustness and significantly reducing chattering.

11. 221: "Assumptions 1–4": shouldn't this be 1–3 instead?

    Response: Thank you for catching this. You are correct that only Assumptions 1–3 are stated. We have now corrected the text.

12. 227: Proof of Theorem 1 is central to the theoretical study, yet difficult to understand because too concise in my opinion. It is unclear how the delta(t) term comes back into play to ensure the claimed robustness, especially because this term was set to zero in several steps of the reasoning. It would benefit from further development, perhaps in an appendix. *Response:* Thank you for your remark. We are fully aware with you and have strongly modified the proof in order to improve the understanding of this important point. Thus, the proof of Theorem 1 in the revised version reads now as (see page 11)

    Proof of Theorem 1. The observer (22) has been designed for the system (20) in the $\hat{z}$-state space; the gain L_{ϕ_1} tuning is based on the bound of $\mathcal{F}(\cdot)$. From there, the writing of the observer (22) must be made in the $\hat{x}$-state space. With this objective, consider $\boldsymbol{z} = \boldsymbol{\Phi}(\boldsymbol{x}, \boldsymbol{u})$ that gives

$$\dot{\boldsymbol{z}} = \frac{\partial \boldsymbol{\Phi}}{\partial \boldsymbol{x}} \dot{\boldsymbol{x}} + \frac{\partial \boldsymbol{\Phi}}{\partial \boldsymbol{u}} \dot{\boldsymbol{u}} \tag{26}$$

    So, one has

$$\mathbf{A} \cdot \boldsymbol{z} + \begin{bmatrix} 0 \\ \mathcal{F} \end{bmatrix} = \frac{\partial \boldsymbol{\Phi}}{\partial \boldsymbol{x}} \boldsymbol{f}(\boldsymbol{x}, \boldsymbol{u}) + \frac{\partial \boldsymbol{\Phi}}{\partial \boldsymbol{u}} \dot{\boldsymbol{u}} + \frac{\partial \boldsymbol{\Phi}}{\partial \boldsymbol{x}} \Delta(t) \tag{27}$$

    By considering non-perturbed and perturbed terms in the two state spaces, one has

$$\mathbf{A} \cdot \boldsymbol{z} = \frac{\partial \boldsymbol{\Phi}}{\partial \boldsymbol{x}} \boldsymbol{f}(\boldsymbol{x}, \boldsymbol{u}) + \frac{\partial \boldsymbol{\Phi}}{\partial \boldsymbol{u}} \dot{\boldsymbol{u}} \quad \text{and} \quad \begin{bmatrix} 0 \\ \mathcal{F} \end{bmatrix} = \frac{\partial \boldsymbol{\Phi}}{\partial \boldsymbol{x}} \Delta(t) \tag{28}$$

    From $\hat{\boldsymbol{z}} = \boldsymbol{\Phi}(\hat{\boldsymbol{x}}, \boldsymbol{u})$, an observer of (22) in the $\hat{x}$-state space reads as

$$\begin{aligned} \dot{\hat{\boldsymbol{x}}} &= \left[\frac{\partial \boldsymbol{\Phi}}{\partial \hat{\boldsymbol{x}}}\right]^{-1} \cdot \left(\dot{\hat{\boldsymbol{z}}} - \frac{\partial \boldsymbol{\Phi}}{\partial \boldsymbol{u}} \dot{\boldsymbol{u}}\right) \\ &= \left[\frac{\partial \boldsymbol{\Phi}}{\partial \hat{\boldsymbol{x}}}\right]^{-1} \cdot \left(\mathbf{A}\, \hat{\boldsymbol{z}} + \begin{bmatrix} \gamma_1(\cdot) \\ \gamma_2(\cdot) \end{bmatrix} - \frac{\partial \boldsymbol{\Phi}}{\partial \boldsymbol{u}} \dot{\boldsymbol{u}}\right) \\ &= \left[\frac{\partial \boldsymbol{\Phi}}{\partial \hat{\boldsymbol{x}}}\right]^{-1} \cdot \left(\mathbf{A}\, \hat{\boldsymbol{z}} - \frac{\partial \boldsymbol{\Phi}}{\partial \boldsymbol{u}} \dot{\boldsymbol{u}}\right) + \left[\frac{\partial \boldsymbol{\Phi}}{\partial \hat{\boldsymbol{x}}}\right]^{-1} \cdot \begin{bmatrix} \gamma_1(\cdot) \\ \gamma_2(\cdot) \end{bmatrix} \end{aligned} \tag{29}$$

    From the left-hand side term of (28), the previous system reads as

$$\dot{\hat{\boldsymbol{x}}} = \boldsymbol{f}(\hat{\boldsymbol{x}}, \boldsymbol{u}) + \left[\frac{\partial \boldsymbol{\Phi}}{\partial \hat{\boldsymbol{x}}}\right]^{-1} \cdot \begin{bmatrix} \gamma_1(\cdot) \\ \gamma_2(\cdot) \end{bmatrix} \tag{30}$$

that is the form of system displayed in Theorem 1. Given that system (22) is an observer of (20) under condition (23), then system in (29) is an observer for (8) if condition (25) is fulfilled with $a_1 = 1.5$ and $a_2 = 1.1$. ■

13. Eq. (31)–(32): specify the variables to tune and initialize, along with guidance on selecting appropriate values, so the community can reproduce and compare results.

Response: Thank you for this comment. To address this concern, we have clarified the tunable and initialization parameters associated with the adaptive gain laws, together with guidance on their roles and selection. Specifically, an explanatory paragraph has been added immediately after the adaptive-gain equations to describe the design parameters and their influence on the observer behavior. In addition, a dedicated subsection has been included in the simulation section to explicitly report the numerical values.

After adaptive-gain equations:

with $\psi = \dfrac{\mathrm{d}}{\mathrm{d}t}(\omega_r - \hat{\omega}_r)$, where $\alpha > 0$ and $\varepsilon > 0$ are design parameters of the adaptive law. The parameter ε defines the target accuracy of the rotor speed estimation, while α governs the adaptation rate of the observer gains. The constants $k_1(0) > 0$ and $k_2(0) > 0$ denote the initial values of the adaptive gains.

The adaptation mechanism operates according to the following principle: (i) when the estimation error exceeds the target accuracy, i.e., $|\omega_r - \hat{\omega}_r| > \varepsilon$, the observer gains are increased to improve convergence; and (ii) when the estimation accuracy is sufficient, the gains are decreased to avoid unnecessary amplification of measurement noise.

In simulation results Section:

4.1 Simulation set-up

The simulation environment integrates Matlab/Simulink 2023a for implementing the observers with OpenFAST (Jonkman et al., 2009), which simulates the high-fidelity aero-hydro-servo-elastic model of the FOWT. Each test is run for 800 s under identical wind and wave conditions, with a fixed sampling time of 0.0125 s. Although the observer design is based on the reduced-order model in Eq. (24), all 24 degrees of freedom available in OpenFAST are activated to ensure a comprehensive evaluation under realistic conditions. Realistic turbulent inflow wind fields are generated using TurbSim (Jonkman, 2009) based on the IEC Kaimal turbulence model, with a mean wind speed of 18 m s^{-1}. A logarithmic mean wind profile is employed, resulting in vertical wind shear across the rotor disk. The inflow is prescribed as a full-field turbulent wind to OpenFAST, such that the aerodynamic loads are computed using the spatially varying wind field. For analysis and validation purposes, REWS is considered, while the underlying aerodynamic response is influenced by the full-field inflow. Irregular wave conditions are modeled using the HydroDyn module (Jonkman et al., 2014). The incident wave field is prescribed as a stochastic irregular process with a significant wave height of 3.25 m. Hydrodynamic loads acting on the floating platform are computed using the built-in potential-flow formulation in HydroDyn, based on precomputed WAMIT data. This formulation accounts for linear wave-excitation forces, hydrostatic restoring forces, and radiation effects through

convolution-based memory terms. The hydrodynamic model is fully coupled with the aero-servo-elastic dynamics in OpenFAST, such that wave-induced platform motions interact with the aerodynamic response of the rotor. Both wind and wave conditions are illustrated in Fig. 3. The observer parameters design have been fine-tuned to achieve the best performance as follows: for the constant-gain SOSMO in Eq. (24), the coefficients are set following (Levant, 2003) to $a_1 = 1.5$ and $a_2 = 1.1$, and the gain is selected as $L_{\phi_1} = 0.01$; for the adaptive-gain observer (ASOSMO) in Eqs. (32)–(33), the design parameters are chosen as $\alpha = 10^{-4}$ and $\varepsilon = 10^{-3}$, with initial values $k_1(0) = 0.1$ and $k_2(0) = 10^{-4}$.

14. 271: it should be mentioned that the simulation result is in zone (III) and that other regimes are covered in the experimental section.

    Response: Thank you for this suggestion. We have clarified the operating regime of the simulations by adding the following sentence at the beginning of Sect. 4 on page 14:

    In this section, the performances of the proposed wind speed observers are evaluated and compared with the CD-EKF used in ROSCO, which is described in Appendix A. All simulations are conducted on the NREL 5 MW FOWT, supported by a semi-submersible platform. The simulation study in this section is conducted in the above-rated operating regime (Region III). Other operating regimes are covered in the experimental validation section (Sect. 5).

15. 276: is there vertical shear in the TurbSim wind? More details on the model fidelity would be appreciated. Same for the hydrodynamic part.

    Response: Yes. The turbulent inflow wind fields are generated with TurbSim as *full-field* wind inputs based on the IEC Kaimal model, and we include vertical shear by applying a logarithmic mean wind profile across the rotor disk. As a result, the aerodynamic loads in OpenFAST are computed from a spatially varying wind field (including shear and turbulence), while the performance evaluation is reported in terms of the REWS derived from that full-field inflow.
    Regarding model fidelity, all 24 degrees of freedom of OpenFAST are enabled (aero-servo-elastic + platform dynamics) to ensure a high-fidelity benchmark. For the hydrodynamics, irregular waves are simulated using HydroDyn with a potential-flow formulation based on precomputed WAMIT data. This includes linear wave excitation, hydrostatic restoring, and radiation effects (via convolution/memory terms), fully coupled with the aero-servo-elastic system such that wave-induced platform motions affect the aerodynamic response. We have expanded Sect. 4.1 to explicitly state these wind-shear and hydrodynamic-modeling choices and to clarify how they contribute to the overall simulation fidelity.

16. 307: lower cost: this is supported by metrics given later in 4.2 so this statement comes

too early. Consider moving it.

Response: We agree that the statement regarding lower computational cost could state later. The sentence has been revised to focus solely on estimation accuracy, and the discussion of computational cost has now been moved to Sect. 4.4, where it is explicitly supported by quantitative execution-time metrics.
The revised sentence now reads as
The findings ~~demonstrate~~ illustrate the efficacy of sliding mode-based observers in enhancing estimation accuracy. ~~while preserving a lower computational cost.~~

17. 311: "under varying wind scenarios": what are these? Only one main scenario appears in 4.1.

    Response: Thank you for the comment. The sentence has therefore been removed to avoid any ambiguity.

18. Overall comment on section 4: to capture the inherent stochastic aspect of (simulated) wind and assess sensivitiy to model fidelity, more scenarios would need to be run, possibly using other wind generation models. This would illustrate how SOSMO and ASOSMO compare to CD-EKF and provide a statistical view of the performance. The authors could consider a separate publication focused solely on simulation results to achieve these purposes. Section 4 is valuable but would benefit from more content. More generally, it raises the question of whether Section 4 has an added value and if Section 5 might suffice on its own, thereby freeing space for more details in other sections.

    Response: We thank the reviewer for this comment regarding the scope and added value of Section 4. To address this concern, we have added a new dedicated Monte Carlo (MC) analysis subsection in Section 4, which quantifies sensitivity to initialization errors and introduces a convergence-time metric. This MC analysis provides a statistical measure and complements the deterministic simulation cases by enabling a controlled comparison between SOSMO, ASOSMO, and CD–EKF under identical operating conditions. As such, Section 4 now offers added value beyond Section 5.

19. Section 5: a diagram alongside Fig.10 would help clarify which parts are experimental and which are simulated, especially since the observer is in SIL but also a part of the turbine response is provided through OpenFAST. Additionally, it would be useful to indicate the differences between this setup and one where only the observer is in SIL/HIL (i.e. without the turbine response provided by a model.

    Response: Thank you for this comment. In the revised manuscript, a new schematic diagram (Fig. 12) has been added alongside Fig. 10, and Section 5 has been expanded to clearly distinguish which components of the system are reproduced experimentally and which are simulated numerically.
    The experimental setup is designed to reproduce the coupled aero–hydro–servo–elastic

behavior of a floating offshore wind turbine under realistic conditions. In the wave tank, hydrodynamic effects, including wave excitation, platform motions, and mooring-system dynamics, are reproduced physically using a scaled prototype. In contrast, aerodynamic effects are computed numerically in real time through a software-in-the-loop (SIL) implementation of OpenFAST.

5 Experimental results

The proposed observers have been experimentally validated on a SIL setup at École Centrale Nantes, France. The experimental platform consists of a 1/32-scale semi-submersible FOWT, based on the OC4-DeepCwind concept, deployed in the wave tank of the LHEEA Laboratory (LHEEA Laboratory, 2025). The physical model includes the floating platform, tower, and mooring system and is instrumented with motion-tracking markers and load sensors, as shown in Fig. 10. This setup provides realistic hydrodynamic excitation through physical wave generation and platform motion.

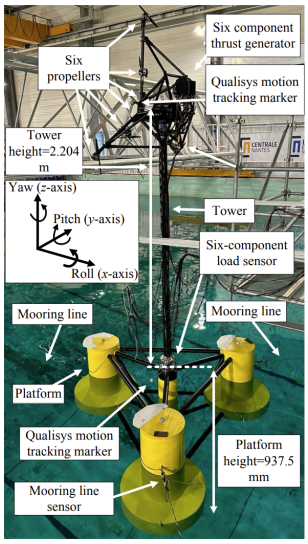

Figure 11: Experimental SIL test setup of the 5 MW 1/32-scale semi-submersible OC4 FOWT at *École Centrale Nantes* (Aslmostafa et al., 2026).

The overall SIL architecture is illustrated in Fig. 12. In this hybrid configuration, the hydrodynamic processes, wave excitation, viscous and radiation loads, mooring-line forces, and the resulting platform dynamics are reproduced physically in the wave tank. Consequently, the corresponding hydrodynamic modules of OpenFAST (HydroDyn, MAP++, MoorDyn or FEAMooring, ElastoDyn), highlighted in the blue dashed region of Fig. 12, are disabled in the numerical simulation. Instead, the measured 6 degrees of freedom platform and tower-top motions from the Qualisys system are imposed as inputs to the real-time numerical model (Bonnefoy et al., 2024). It should be noted that aerodynamic loads are computed numerically. In other words, a modified real-time implementation of OpenFAST runs, where the wind field is prescribed numerically and the aerodynamic modules (InflowWind, AeroDyn, ServoDyn), highlighted in the red dashed region of Fig. 12,

remain active. At each iteration of the SIL loop, the solver receives the measured motions and computes the instantaneous aerodynamic thrust corresponding to the imposed wind field. This thrust is then applied to the physical model by a tower-top actuator system (Fig. 11), enabling consistent aero-hydro coupling during the experiment.

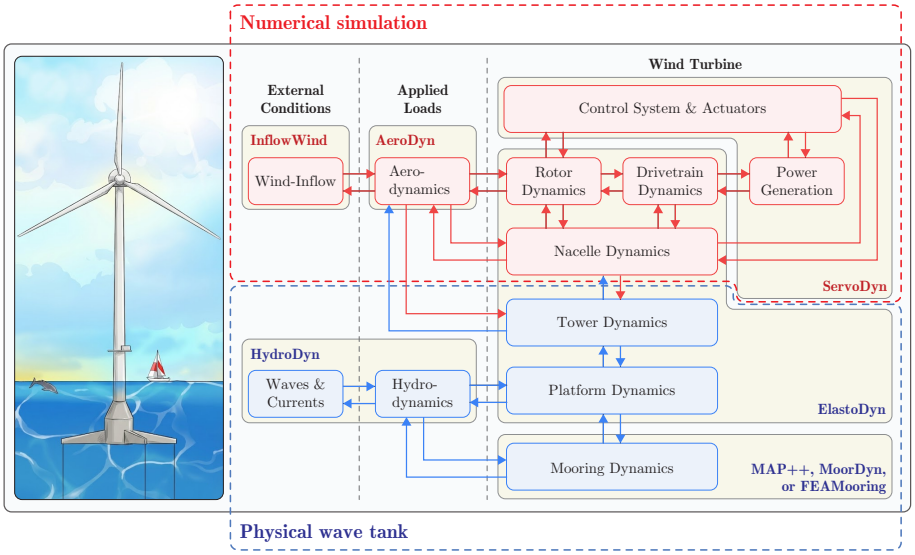

Figure 12: Schematic of the modules in the SIL architecture. The figure is inspired by Bonnefoy et al. (2024) and National Renewable Energy Laboratory (2023). The hydrodynamic and structural modules (blue dashed region) are disabled, as the corresponding processes are reproduced physically in the wave tank, while the aerodynamic modules (red dashed region) remain active and compute real-time aerodynamic loads using the prescribed wind field and measured platform motions.

In the SIL setup, the inflow wind field is numerically prescribed in OpenFAST. Based on this inflow and the instantaneous platform and rotor conditions, OpenFAST computes the corresponding REWS $v_r(t)$, which is used as the reference signal for evaluating the estimation error.This approach allows the observer to be tested under realistic platform motions and hydrodynamic conditions, i.e., under realistic physical disturbances.

20. Sections 4–5: clarify why the figures show rotor speed estimations while the observers are described as using rotor speed measurements as input (therefore not requiring estimation).

Response: We thank the reviewer for this remark. Although rotor speed is directly measured and used as an input to the observer, it is also reconstructed internally in order to explicitly verify the convergence properties of the observer. In the proposed framework, convergence of the reconstructed rotor speed $\hat{\omega}_r$ toward the measured rotor speed ω_r is a necessary condition for correct rotor-effective wind speed estimation.
Owing to the nonlinear coupling between rotor speed and wind speed in the aerodynamic torque expression, once $\hat{\omega}_r \to \omega_r$, observability of the reduced-order model ensures that the wind speed estimate also converges, *i.e.*, $\hat{v}_r \to v_r$.
The observer therefore does not estimate rotor speed to compensate for missing mea-

surements, but rather to verify convergence and to validate the estimation mechanism.

21. 321: thrust generation by the fans and the connection with OpenFAST could be better explained, possibly with a diagram.

    Response: We thank the reviewer for this helpful comment. In the revised manuscript, we have improved the textual explanation in Section 5 by explicitly describing the real-time interaction between OpenFAST and the experimental setup. In particular, we now clearly state that aerodynamic loads are computed numerically within OpenFAST from the prescribed wind field and the measured platform motions, and that the resulting aerodynamic thrust is applied to the physical model through the nacelle-mounted fan system. The measured structural motions are then fed back to OpenFAST, closing the aero–hydro coupling loop.

22. Fig 11: ASOSMO exhibits what appears to be a transient response in [0;50] s. Are performance metrics calculated excluding the transients (for all algorithms)?

    Response: Thank you for this insightful observation.
    The transient behavior observed for the ASOSMO during the initial time corresponds to the gain adaptation phase inherent to the adaptive supertwisting structure. During this short period, the observer gains are adjusted online to reach appropriate values that balance convergence speed and robustness, while avoiding excessive gain overestimation that could negatively affect performance.
    It is important to note that this transient has a limited impact on the REWS estimation, which is the main variable of interest in this study. The initial time window was selected to ensure stable and reliable estimation behavior. To further assess the sensitivity to the choice of the initial time, an additional MC analysis investigating different initial transient durations has been added in Section 4.3 on page 18.
    Regarding the performance metrics, all quantitative results are computed over the same time interval for all three observers. This ensures a fair and consistent comparison. Moreover, the performance metrics are calculated only for the REWS, not for the rotor speed, in accordance with the primary objective of the paper.

23. 357–358: while no covariance matrix tuning is necessary, consider adding details on the tuning of the observers for a fair comparison.

    Response: Thank you for this suggestion. In the revised manuscript, we added explicit details on the tuning/parameter selection of the proposed observers to ensure a fair comparison with the CD-EKF. Specifically, in the newly added on page 14 as
    4.1 Simulation set-up
    The observer parameters design used in the simulations are specified as follows: for the constant-gain SOSMO in Eq. (24), the coefficients are set following (Levant, 2003) to

$a_1 = 1.5$ and $a_2 = 1.1$, and the gain is selected as $L_{\phi_1} = 0.01$; for the adaptive-gain observer (ASOSMO) in Eqs. (32)–(33), the design parameters are chosen as $\alpha = 10^{-4}$ and $\varepsilon = 10^{-3}$, with initial values $k_1(0) = 0.1$ and $k_2(0) = 10^{-4}$.

In addition, we expanded the description of the CD-EKF to clarify its tuning requirements. In the CD-EKF results/discussion part as

The practical implementation of the CD-EKF requires careful tuning of the process-noise and measurement-noise covariance matrices $\mathbf{Q}$ and R_m, which constitute the main design parameters of the filter, as well as linearization of the system dynamics. In the present formulation (see Appendix A), this corresponds to tuning four parameters, namely the diagonal entries of $\mathbf{Q}$ associated with the rotor speed state, the turbulent wind component, and the mean wind component, together with the measurement-noise variance R_m. These parameters are selected based on sensor characteristics, turbulence modeling considerations, and empirical adjustments to ensure filter stability and satisfactory estimation performance.

As commonly reported in the literature, the estimation performance of EKF-based approaches is sensitive to the choice of these covariance parameters. Moreover, no systematic or universal tuning procedure exists for their selection, which represents a well-known practical limitation of Kalman-filter-based methods, particularly for highly nonlinear and uncertain systems such as FOWT.

24. 362–363: "system stability and reduced fatigue loads" is this implicitly about a feedfoward control strategy? Can the proposed estimation strategy provide a prediction of free wind speed in the next seconds?

    Response: Thank you for this remark. The present work focuses on *estimating* the instantaneous REWS using second-order sliding-mode observers. We do *not* design or implement a specific feedforward control strategy in this paper, and the proposed observers do *not* provide an explicit prediction of the free-stream wind speed in the next seconds; they estimate the current REWS from the measured rotor speed.

    Our statement about "improved system stability and reduced fatigue loads" is intended to refer to the *potential* benefits when the proposed wind speed estimator is integrated into suitable control schemes (for example, pitch and/or torque control).

Technical corrections

Suggested modifications: (square brackets for insertion, double dash for removal)

Response: We thank the reviewer for the careful reading of the manuscript. We appreciate these helpful technical corrections. All suggested modifications have been addressed in the revised version of the manuscript.

1. 100: "a software-in-the-loop [setup] located in LHEEA lab" → ✓
2. 117: "such as Betz's law" > "reported by Betz's law" → ✓

3. 127: “taking into account -for- blade” → ✓
4. 134: “control vector [u]” → ✓
5. 139: “unknown[, which] gives” → ✓
6. 188: “-It is why- However, the previous” → Thank you for highlighting this point. While we agree that the phrase “It is why” was inappropriate, we found that “However” introduced an unintended contrast. To maintain a smoother flow and preserve the intended meaning, we opted “Therefore.”
7. 204: “-one- transformation” → ✓
8. 214: “cannot” → ✓
9. 249: “-phenomenon-” → ✓
10. 254: “large enough” → ✓
11. Sections 4–5: consider making figures that use the full width of the pages and possibly with increased height. → Thank you for this suggestion. Although full-page figures were technically possible, we chose to keep them in a single-column width (based on WES guidelines) because the manuscript contains a large number of results (especially after revised version).
12. 303: “-The- both” → ✓
13. 306: “the findings -demonstrate- illustrate the efficacy” → ✓
14. 354: “-validated- evaluated” → ✓

Concluding Remarks

We again thank the reviewers for their valuable insights. We believe the manuscript has been significantly improved in response to these comments.

Sincerely,
Authors

References

Aslmostafa, E., Mirzaei, M., Hamida, M., and Plestan, F.: Experimental evaluation of robust nonlinear control strategies for regions II and III for floating offshore wind turbines, Ocean Engineering, 346, 123 887, 2026.

Bonnefoy, F., Leroy, V., Mojallizadeh, M., Delacroix, S., Arnal, V., and Gilloteaux, J.-C.: Multidimensional hybrid software-in-the-loop modeling approach for experimental analysis of a floating offshore wind turbine in wave tank experiments, Ocean Engineering, 309, 118 390, 2024.

Burton, T., Jenkins, N., Sharpe, D., and Bossanyi, E.: Wind Energy Handbook, John Wiley & Sons, Ltd, 2011.

Gräfe, M., Pettas, V., Gottschall, J., and Cheng, P. W.: Quantification and correction of motion influence for nacelle-based lidar systems on floating wind turbines, Wind Energy Science, 8, 925–946, 2023.

Guo, F. and Schlipf, D.: Assessing lidar-assisted feedforward and multivariable feedback controls for large floating wind turbines, Wind Energy Science, 8, 1299–1317, 2023.

Guo, F., Schlipf, D., and Cheng, P. W.: Evaluation of lidar-assisted wind turbine control under various turbulence characteristics, Wind Energy Science, 8, 149–171, 2023.

Harris, M., Hand, M., and Wright, A.: Lidar for turbine control, National Renewable Energy Laboratory, Golden, CO, Report No. NREL/TP-500-39154, 2006.

He, S., Wang, B., and Chen, Y.: Improved optimal torque control for large scale floating offshore wind turbines based on interval type-2 fuzzy logic system, Ocean Engineering, 330, 121 186, 2025.

Isidori, A.: Nonlinear Control Systems, Springer London, ISBN 978-1-84628-615-5, 1989.

Jena, D. and Rajendran, S.: A review of estimation of effective wind speed based control of wind turbines, Renewable and Sustainable Energy Reviews, 43, 1046–1062, 2015.

Jonkman, B. J.: TurbSim user's guide: Version 1.50, Tech. rep., National Renewable Energy Laboratory, Golden, CO (United States), 2009.

Jonkman, J., Butterfield, S., Musial, W., and Scott, G.: Definition of a 5-MW Reference Wind Turbine for Offshore System Development, National Renewable Energy Laboratory, 2009.

Jonkman, J. M., Robertson, A. N., and Hayman, G. J.: HydroDyn User's Guide and Theory Manual, Tech. rep., National Renewable Energy Laboratory, Golden, CO (United States), 2014.

Levant, A.: Sliding order and sliding accuracy in sliding mode control, International Journal of Control, 58, 1247–1263, 1993.

Levant, A.: High-order sliding modes: differentiation and output-feedback, Int. J. Control, 76, 924–941, 2003.

Levant, A.: Chattering Analysis, IEEE Transactions on Automatic Control, 55, 1380–1389, 2010.

LHEEA Laboratory: LHEEA Laboratory - École Centrale de Nantes, `https://lheea.ec-nantes.fr/`, 2025.

Li, J. and Geng, H.: Platform Pitch Motion Suppression for Floating Offshore Wind Turbine in Above-Rated Wind Speed Region, IEEE Transactions on Sustainable Energy, 15, 1994–2005, 2024.

Ma, R., Siaw, F. L., Thio, T. H. G., and Yang, W.: New adaptive super-twisting extended-state observer-based sliding mode scheme with application to fowt pitch control, Journal of Marine Science and Engineering, 12, 902, 2024.

Mahdizadeh, A., Schmid, R., and Oetomo, D.: LIDAR-Assisted Exact Output Regulation for Load Mitigation in Wind Turbines, IEEE Transactions on Control Systems Technology, 29, 1102–1116, 2021.

Manwell, J. F., McGowan, J. G., and Rogers, A. L.: Wind energy explained: Theory, design and Application, Wiley, Chichester, U.K., 2009.

Moldenhauer, R. H. and Schmid, R.: Lidar-assisted nonlinear output regulation of wind turbines for fatigue load reduction, Wind Energy Science, 10, 1907–1928, 2025.

National Renewable Energy Laboratory: OpenFAST Documentation, `https://openfast.readthedocs.io`, accessed: 2026-01-12, 2023.

Schlipf, D., Guo, F., Raach, S., and Lemmer, F.: A Tutorial on Lidar-Assisted Control for Floating Offshore Wind Turbines, in: 2023 American Control Conference (ACC), pp. 2536–2541, 2023.

Shu, Z., Li, Q., He, Y., and Chan, P.: Observations of offshore wind characteristics by Doppler-LiDAR for wind energy applications, Applied Energy, 169, 150–163, 2016.

Simley, E., Bortolotti, P., Scholbrock, A., Schlipf, D., and Dykes, K.: IEA Wind Task 32 and Task 37: Optimizing Wind Turbines with Lidar-Assisted Control Using Systems Engineering, Journal of Physics: Conference Series, 1618, 042 029, 2020.

Soltani, M. N., Knudsen, T., Svenstrup, M., Wisniewski, R., Brath, P., Ortega, R., and Johnson, K.: Estimation of Rotor Effective Wind Speed: A Comparison, IEEE Transactions on Control Systems Technology, 21, 1155–1167, 2013.

Svenstrup, M. A. and Thomsen, J. S.: Robustness of LiDAR-assisted controller towards measurement uncertainty, Journal of Physics: Conference Series, 2767, 032 052, 2024.

Woolcock, L., Liu, V., Witherby, A., Schmid, R., and Mahdizadeh, A.: Comparison of REWS and LIDAR-based feedforward control for fatigue load mitigation in wind turbines, Control Engineering Practice, 138, 105 477, 2023.